Acta Biomaterialia 100 (2019) 18–28

Contents lists available at ScienceDirect

Acta Biomaterialia

journal homepage: www.elsevier.com/locate/actbio

Full length article

Matrix-induced pre-strain and mineralization-dependent interfibrillar shear transfer enable 3D fibrillar deformation in a biogenic armour

Yanhong Wang[a], Yi Zhang[b], Nicholas J. Terrill[c], Ettore Barbieri[d], Nicola M. Pugno[e,a,f], Himadri S. Gupta[a,*]

[a] School of Engineering and Materials Science and Institute of Bioengineering, Queen Mary University of London, London E1 4NS, United Kingdom
[b] Institute of High Energy Physics, Chinese Academy of Science, Beijing, China
[c] Diamond Light Source, Harwell Science and Innovation Campus, Didcot, Harwell OX11 0DE, United Kingdom
[d] Japan Agency for Marine-Earth Science and Technology (JAMSTEC), Research Institute for Value-Added-Information Generation (VAiG), Center for Mathematical Science and Advanced Technology (MAT), 3173-25, Showa-machi, Kanazawa-ku, Yokohama-city, Japan
[e] Laboratory of Bio-Inspired & Graphene Nanomechanics, Department of Civil, Environmental and Mechanical Engineering, University of Trento, Via Mesiano, 77, 38123 Trento, Italy
[f] Ket Lab, Edoardo Amaldi Foundation, Via del Politecnico snc, 00133 Rome, Italy

ARTICLE INFO

Article history:
Received 12 April 2019
Revised 19 September 2019
Accepted 24 September 2019
Available online 26 September 2019

Keywords:
Chitin-based biomaterials
Nanoscale mechanics
In situ synchrotron wide-angle X-ray diffraction
Fibrillar deformation
Arthropod cuticle

ABSTRACT

The cuticle of stomatopod is an example of a natural mineralized biomaterial, consisting of chitin, amorphous calcium carbonate and protein components with a multiscale hierarchical structure, and forms a protective shell with high impact resistance. At the ultrastructural level, cuticle mechanical functionality is enabled by the nanoscale architecture, wherein chitin fibrils are in intimate association with enveloping mineral and proteins. However, the interactions between these ultrastructural building blocks, and their coupled response to applied load, remain unclear. Here, we elucidate these interactions via synchrotron microbeam wide-angle X-ray diffraction combined with *in situ* tensile loading, to quantify the chitin crystallite structure of native cuticle – and after demineralization and deproteinization – as well as time-resolved changes in chitin fibril strain on macroscopic loading. We demonstrate chitin crystallite stabilization by mineral, seen via a compressive pre-strain of approximately 0.10% (chitin/protein fibre pre-stress of ~20 MPa), which is lost on demineralization. Clear reductions of stiffness at the fibrillar-level following matrix digestion are linked to the change in the protein/matrix mechanical properties. Furthermore, both demineralization and deproteinization alter the 3D-pattern of deformation of the fibrillar network, with a non-symmetrical angular fibril strain induced by the chemical modifications, associated with loss of the load-transferring interfibrillar matrix. Our results demonstrate and quantify the critical role of interactions at the nanoscale (between chitin-protein and chitin-mineral) in enabling the molecular conformation and outstanding mechanical properties of cuticle, which will inform future design of hierarchical bioinspired composites.

Statement of Significance

Chitinous biomaterials (e.g. arthropod cuticle) are widespread in nature and attracting attention for bioinspired design due to high impact resistance coupled with light weight. However, how the nanoscale interactions of the molecular building blocks – alpha-chitin, protein and calcium carbonate mineral – lead to these material properties is not clear. Here we used X-ray scattering to determine the cooperative interactions between chitin fibrils, protein matrix and biominerals, during tissue loading. We find that the chitin crystallite structure is stabilized by mineral nanoparticles, the protein phase prestresses chitin fibrils, and that chemical modification of the interfibrillar matrix significantly disrupts 2D mechanics of the microfibrillar chitin plywood network. These results will aid rational design of advanced chitin-based biomaterials with high impact resistance.

* Correspondence author.
E-mail addresses: yanhong.wang@qmul.ac.uk (Y. Wang), zhangyi88@ihep.ac.cn (Y. Zhang), nick.terrill@diamond.ac.uk (N.J. Terrill), e.barbieri@jamstec.go.jp (E. Barbieri), nicola.pugno@unitn.it (N.M. Pugno), h.gupta@qmul.ac.uk (H.S. Gupta).

https://doi.org/10.1016/j.actbio.2019.09.036
1742-7061/

1. Introduction

Biological structural materials have – due to the optimization of structure to function during evolution – been brought into focus, either directly modified as multifunctional composites or used as templates and inspiration to design advanced synthetic biomaterials [1–6]. Fibre-based composites with hierarchical organization at multiple length scales – including arthropod exoskeletons, wood, bone, and shells – are prototypical examples [7,8]. The mechanical properties of these hierarchical composites originate from a combination of the properties of the supramolecular fibre-matrix building block, together with biologically-driven structural variations of this motif at micro- and macro-length scales [8,9]. The intrinsically complex supramolecular building-block is formed via an intimate association of organic crystalline nanofibrils, surrounding layers of thin, confined amorphous matrices of proteins or polysaccharides, and inorganic bio-minerals like calcium carbonate or calcium phosphate variants [10–12]. The mechanical properties of such complex nanostructured systems, not easily predictable from bulk phase measurements, are important for next-generation structural biomaterials design and function [4]. Therefore, determining the nanoscale mechanics – in particular, the strain and structure of the nanofibrous phase – in such hierarchical nanocomposite materials is essential (but technically challenging) to shed light on the small-scale interactions between the ultrastructural building components which enable multiple functionalities.

The exoskeleton of arthropod is a multiscale biological material, comprised of a chitin-based fibrillar network and reinforced by the incorporation of biomineral particles (Fig. 1g) [13–20]. These chitin fibrils form a characteristic rotated layered plywood (Bouligand) structure at the scale of $\sim 10 \mu$m, which develops into a well-defined honeycomb lattice-like system with pore canal running perpendicular to these lamellae [21,22]. Similar to the hard tissues, including vertebrate bones [23,24] and tooth dentin [25], stomatopod (also known as mantis shrimp, e.g. *Odontodactylus scyllarus*) cuticle is an example of mineralized crustacean exoskeleton, which, at the nanometre level, can be described as a combination of organic phase (chitin and protein) and inorganic mineral phase (principally amorphous calcium carbonate (ACC), with a small amount of amorphous calcium phosphate (ACP) and calcite) [26–28]. Mineral takes up about 67% of the dry cuticle whereas chitin-protein organic occupies around 33% (mantis shrimp saddle [26]), but these vary in different species of animals. The high dynamic mechanical properties and impact resistance of specialized adaptations of cuticle (e.g. in stomatopod raptorial appendages [16,29] and telson [30]) also depend – at the nanometer scale – principally on the arrangements and the interactions of these constituents - chitin fibrils, proteins, and minerals.

Such intimate nanoscale interactions have functional consequences in biomechanically important tissues [31–33]. The interaction of the chitin and protein was explored using biochemical methods [34,35], molecular simulations [36,37] and X-ray diffraction [12,38]. From a biochemical viewpoint, some proteins were bonded into chitin with an extended form of a R&R sequence (a 35–36 amino acid motif with a single, conserved domain) [34], as well as a chitin-protein bonding through hydrogen bonds affected by the presence of water molecule [36,37]. Regarding the orthorhombic crystal structure of chitin, the lattice spacings facilitate interactions of the protein with fibrous chitin. Specifically, the spacing along the *a*-axis of 0.475 nm in chitin was the same as the distance between the adjacent protein chains in a β-sheet arrangement. Further, twice the lattice spacing along the *c*-axis of chitin (2.064 nm) is close to three times the 0.69 nm repeat (2.07 nm) along the protein chains [39]. Synchrotron X-ray diffraction and modelling on spider tendon, in native and deproteinized states, provided evidence of strong protein/chitin and water/chitin interactions [12]. Nevertheless, we do not know in detail the role of the proteins in the interactions with the chitin crystalline structure, and also have very little quantitative information on the *in situ* nanoscale mechanics in biomineralized stomatopod cuticle.

Evidence exists of interaction between organic molecules and the biogenic minerals – within this broad framework - using X-ray diffraction [11,40], where the organic molecules, orienting to a specific crystallographic plane, induced anisotropic lattice distortions in biogenic calcite with a strain reaching up $\sim$0.2% along the *c*-axis [40]. In some other biological materials, the collagen contraction during biomineralization or heating-associated dehydration, can change the lattice parameter and cause a compression-like strain (1% in turkey leg tendon [41] vs 0.3% in human tooth dentin [25]) on the mineral particles. Further, the mineral affects the stiffness of mineralized composites, such as bone [42,43] and arthropod cuticle [44,45] with relatively low mineralization leading to a lower elastic modulus, and higher moduli in higher mineralized regions.

However, while the properties and interaction of chitin fibrils, mineral, and protein are believed to be critical to the mechanical properties of cuticle, quantitative experimental measurements of the nanoscale deformation mechanisms in cuticle, and how they change on varying the matrix composition, are lacking. Time-resolved synchrotron X-ray diffraction, combined with *in situ* mechanical testing, can measure the chitin molecular lattice spacing and fibril-level deformation mechanisms (Fig. 1e), as has been shown in bone and tendon before [41,42], and on native (non-modified) cuticle [28]. Modification of the non-chitinous matrix can be done via chemical or enzymatic means [12,38,46–51]. Demineralization protocols usually involve treatment with HCl or another acid [46–48], whilst deproteinization has utilized alkaline agents like NaOH or KOH [12,38,46–48], often at relatively high temperatures (70 °C and above). More recently, milder protocols (to minimize structural damage and deacetylation in chitin during the treatment) have used similar chemicals but at room temperatures over several days, to remove the mineral and protein phase [49–51]. A summary of these approaches is given in Table 1.

In this study, we analyze how the nanoscale deformation mechanisms in stomatopod cuticle change with modifications of the mineral/protein inter-fibre matrix, by a combination of mild room temperature chemical modification, time-resolved synchrotron wide-angle X-ray diffraction (WAXD) together with *in situ* mechanics. Using the (002) *c*-axis diffraction peak as a measure of the axial molecular spacing in chitin fibrils, and its changes with load or chemical modification as indication of changes in fibrillar strain, we analyze the differences in chitin fibrillar spacing and stress/fibrillar-strain relations in control, demineralized (DM) and demineralized/partially deproteinized (DM-DP) cuticle tissue from stomatopod tergite. We use these results to quantify the basic structure-function relations of chitin fibrils and other components (mineral, protein and water) in cuticle.

2. Materials and methods

2.1. Sample preparation

Adult mantis shrimps (non-moulted, i.e. animal in intermoult; *Odontodactylus Scyllarus*, Fig. 1a), were obtained from a local supplier and dissected. The tergite cuticle (Fig. 1b), after the organic tissues removed, was sectioned into strips along the longitudinal axis of the animal with a width of $\sim$0.5 mm using a low-speed diamond blade saw (Buehler Isomet, Buehler, Duesseldorf, Germany).

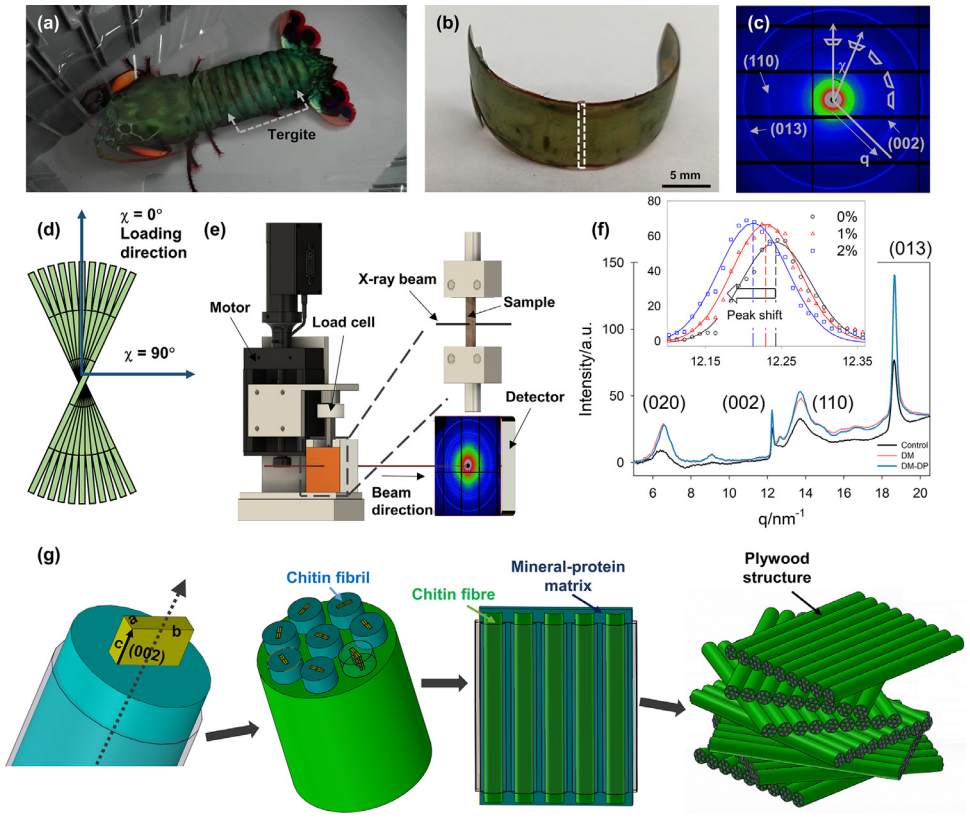

Fig. 1. Experimental setup for *in situ* nanomechanical analysis of chitin fibrils and hierarchical structure of stomatopod cuticle. (a) Picture of a stomatopod. (b) Image of an abdominal segment. The dashed line indicates the section location for tensile cuticle samples. (c) Representative WAXD pattern from stomatopod cuticle with trapezoids indicating the sectors from different sublayers. (d) A combination of chitin fibrils at different sublamellae in a plywood arrangement with angles (χ) to the direction of the applied strain. (e) A schematic of the micromechanical tester used in line with the X-ray beam to simultaneously measure the lattice spacing and the changes in fibril strain when tensile testing performed. (f) 1D intensity profile I(q) showing the typical diffraction peaks in chitin fibril from the control, DM and DM-DP groups. The peak shift of (002) diffraction (inset) is used to determine the fibril strain during mechanical testing. (g) Schematic of structural hierarchy at multiple lengths in cuticle showing the crystal structure of chitin, chitin nanofibrils wrapped with protein, parallel-arranged chitin fibres surrounded by protein-mineral matrix and the twisted plywood architecture of chitin fibre planes.

Table 1
Chemical treatment protocols used to demineralize and deproteinize chitin containing tissues, including cuticle and spider leg.

Tissue source	Demineralization	Deproteinization	Deproteinization temperature (°C)	References
Lobster *Homarus americanus*	3 M HCl	5% KOH	100 °C	Minke and Blackwell [46]
Ovipositor of the Ichneumon Fly *Megurhyssa*	–	5% NaOH	100 °C	Blackwell and Weih [38]
Spider leg	–	40% KOH+ 0.3% NaClO	70 °C	Serrano, Leemreize et al. [12]
Crab cuticle	boiled 0.1 N HCl	40% KOH+ 0.3% NaClO	70 °C	Sikorski, Hori et al. 2009 [47], Ogawa, Hori et al. [55]
Shrimp cuticle	0.25 M HCl	1 M NaOH	70 °C	Percot, Viton et al. [48]
Crab cuticle	1 N HCl	5% NaOH	65 °C	No and Hur
Crab shell	7% HCl	5% NaOH	Room temperature	Ifuku, Nogi et al. [50]
Prawn shell	2 N HCl	1 N NaOH	Room temperature	Ifuku, Nogi et al. [49]
Lobster cuticle	2 M HCl	8% or 20% NaOH	Room temperature	Mushi, Butchosa et al. [51]

2.2. Demineralization and deproteinization protocols

The demineralization and deproteinization protocols followed the room-temperature procedure described in [51]. For demineralization (DM-), the cuticle samples were immersed in 2 M HCl for 2 h under constant stirring, and then immersed in deionized water for 30 mins to remove any residual ions from the solution. Partially deproteinized cuticle (DM-DP-) was obtained by immersing the DM-treated cuticle into 20% NaOH aqueous solution (6.1 M) for two weeks at ambient temperature under constant stirring, and then washing in deionized water overnight. All samples – untreated (control or native), DM- and DM-DP-treated cuticle – were stored at −20 °C for subsequent *in situ* mechanical testing with synchrotron microfocus WAXD. Thermogravimetric-analysis data on cuticles from control, DM and DM-DP groups is shown in Supplementary Figure S1.

2.3. Micromechanical testing

Tensile testing was performed on the cuticle samples during *in situ* synchrotron WAXD measurements, to characterize mechanical differences in the untreated, DM- and DM-DP-treated cuticle. To obtain tissue stresses, sample dimensions were measured using Vernier calipers after defrosting and rehydration. The cuticle

samples were fixed between two grips (gauge length of ~3 mm) with both ends clamped between sandpaper coated grips in a custom-made micromechanical tester (Fig. 1e) with an 110 N load cell (RDP Electronics, UK), a DC motor (M126.DG, Physik Instrumente, UK) and a LabVIEW control interface (National Instruments, UK), developed by our group for biological tissues [28,52]. The chamber was half-filled with water to keep the tissue hydrated during testing. Partial immersion was necessary to keep water level below the X-ray beam position. A 0.1 N tare load was initially applied to the samples, followed by a stretch-to-failure at a constant velocity of 0.0015 mm/s (corresponding to motor-driven grip-displacement strain rate of 0.05%/s). Due to machine compliance effects and shearing at the grip/sample interface, the tissue strain ε_T is smaller than the strain measured by motor-driven grip-displacement. We have previously used a CCD camera and LabVIEW digital image correlation program to measure tissue strain from the relative displacement of two fiducial markers placed on the ends of the sample [53,54]. In the current experiment, it was not possible to measure tissue strain directly during the synchrotron tests, due to limited space to view the sample laterally on the synchrotron sample stage. Therefore, to link motor strain to tissue strain, we carried out lab- (not synchrotron-) tests, where we measured tissue and motor strain simultaneously [28,53]. A linear correlation between tissue strain and motor strain was observed (Supplementary Figure S2), with an average value for the slope of 0.29. Motor strains measured during the synchrotron tests were multiplied by this factor to convert to tissue strain. The tissue modulus (E_T) was calculated from the slope of tissue stress – tissue strain curve, in the elastic region. Scanning electron microscopy (SEM) images of the fracture surface of tensile-tested samples, showing the pore-canal, out-of-plane fibres and honeycomb structure (as reported for lobster cuticle earlier [22]) are shown in Supplementary Figure S4.

2.4. In situ *synchrotron WAXD*

WAXD experiments were conducted on the customised micromechanical tester described above, mounted on the microfocus end-station at the SAXS/WAXD beamline I22 at Diamond Light Source (DLS, Harwell Science and Innovation Campus, UK). Simultaneous WAXD measurements were carried out during *in situ* mechanical testing of the samples, using a 15 µm beam (14 keV). A Pilatus P3-2 M detector, with a pixel size of 172 µm and a resolution of 1475 × 1679 pixels (horizontal & vertical), was used to record WAXD patterns during *in situ* testing. The natural surface of the cuticle was oriented perpendicular to the X-ray beam, i.e. in transmission-geometry both the outer (exocuticle) and inner (endocuticle) contribute to the total WAXD intensity. The sample-to-detector distance (265.4 ± 0.5 mm) was calibrated using silver behenate (AgBe).

WAXD patterns were collected first before loading with a 1 s exposure time and then continuously up to failure of the specimen, with an interval between acquisitions of 5 s. To minimize radiation exposure of the tissue, a vertical offset (10 µm) in sample position (via programmed movement of the mounting-stages) was implemented between each WAXD acquisition via the General Data Acquisition (GDA, http://www.opengda.org) beamline control system, such that a different region was exposed for each WAXD measurement; this is facilitated by the homogeneity of the cuticle transverse to the beam.

2.5. *WAXD data analysis*

To determine the lattice spacing and loading induced deformation, the (002) chitin diffraction peak, oriented along the chitin axis (and fibril axis) [28,55], was used to obtain the lattice spacing $D_{(002)}$ and fibril-strain of chitin fibrils at the nanoscale. The Bouligand (plywood) arrangement of fibrils perpendicular to the X-ray beam results in a ring of diffracted intensity on the WAXD detector (Fig. 1c). Therefore, to first determine the strains of the fibrils parallel to the loading direction (vertical), a narrow angular sector (10°) on the (002) ring centered on the vertical (loading) direction was selected for each WAXD frame, and the intensity was averaged azimuthally to get a 1D integrated intensity profile I(q) (Fig. 1f). As a second step, when the strain for fibrils at an angle (χ, Fig. 1d) to the loading direction was calculated, angular sectors of diffraction on the (002) ring (Fig. 1c) was used to obtained angularly-resolved fibril strains in the Bouligand layer.

Integrated profiles I(q) were fitted to a Gaussian peak-shape with a linear background to obtain the peak position $q_{(002)}$ and lattice spacing $D_{(002)}$ ($D_{(002)}$ is equal to 2π / $q_{(002)}$). The fibril strain (ε_F) is the percentage change in $D_{(002)}$ induced by the applied external loading during tensile testing, as extensively used for other biomaterials [54,56–58]. The reference $D_{(002)}$ or $q_{(002)}$ used to determine ε_F was the initial value for each sample in the unloaded state. The *Processing* pipeline of the data analysis software DAWN [59,60] was used to perform the integration for all 2D WAXD patterns to produce one-dimensional intensity profiles. These profiles were then fitted to Gaussian peak functions with custom code using the Python nonlinear fitting library *lmfit* [61]. To obtain a parameter that links macroscopic stress to nanoscale fibrillar changes, we used the effective fibril modulus, which is the rate of change of tissue stress to fibril strain ($d\sigma_T/d\varepsilon_F$). ($d\sigma_T/d\varepsilon_F$) was calculated from linear regressions of the slope of tissue-level stress to fibril-strain in the elastic region for each sample, as used in prior work [52,54,56].

2.6. *Statistical analysis*

The representative results refer to a single sample, while the grouped data are averaged values with standard deviations. The statistical significance between groups (control, DM and DM-DP) was measured using one-way ANOVA (Sigma Plot, SigmaStat) and indicated at $p < 0.05$ (*), $p < 0.01$ (**), $p < 0.001$ (***) and ns: not significant, followed by Holm–Sidak pairwise tests between groups when the difference was significant ($p < 0.05$). For the angular fibril strains, * were used, in a similar manner, to indicate the statistical significance of the DM- and DM-DP-treated groups relative to the control groups.

3. Results

3.1. *Chemical modification induces significant changes in lattice spacing of chitin fibrils*

A lattice spacing $D_{(002)}$ change in chitin fibrils was produced by chemical modification (demineralization and deproteinization) as shown in Fig. 2. On demineralization (DM), there was a significant ($p < 0.05$) increase in chitin $D_{(002)}$ of approximately 0.10%, from the average value (±standard deviations) of 5.131 Å (±0.003) in the initial native state to 5.136 Å (±0.004) when the mineral was removed from cuticle. This $D_{(002)}$ spacing change corresponds to a compressive lattice pre-strain in the chitin fibrils in the mineralized cuticle (control) as compared with the demineralized samples. On subsequent deproteinization of the demineralized cuticle (DM-DP), $D_{(002)}$ reduced to 5.131 Å (±0.002), a significant ($p < 0.05$) decrease of around 0.1% (~120 MPa) relative to that of the demineralized chitin fibrils. The lattice spacing of chitin in demineralized/partially deproteinized cuticle is not significantly different ($p > 0.05$) from the native cuticle (control) group.

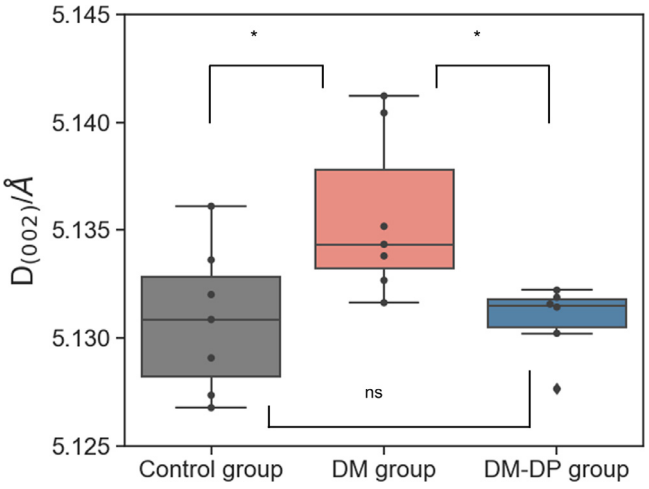

Fig. 2. Chitin fibrils experience an increase in lattice spacing $D_{(002)}$ after demineralization ($p < 0.05$) and then a reduction in response to further deproteinization ($p < 0.05$) for multiple cuticle samples (control $n = 7$, DM $n = 7$, DM-DP $n = 6$). *'s indicates statistical significance between groups (i.e. *: $p < 0.05$; **: $p < 0.01$; ***: $p < 0.001$; ns: not significant). (For interpretation of the references to colour in this figure legend, the reader is referred to the web version of this article.)

3.2. Demineralization and deproteinization lead to altered stress response at macro- and nanoscale

3.2.1. Macroscale mechanics

The cuticle displayed different mechanical responses at both the tissue and fibrillar level after chemical modification (DM and DM-DP) compared to the native cuticle, during stretch-to-failure testing (Fig. 3). Fig. 3a shows the stress response to the applied tissue strain of cuticle samples in control (black), DM (pink) and DM-DP (blue) states. While the statistical comparison will be made subsequently, some general observations can be made here. At a given tissue stress σ_T ~15 MPa, the macroscopic strain ε_T for DM-treated cuticle was ~2%, higher compared with the native cuticle (~0.4%) whilst slightly lower than the DM-DP-treated samples (~2.4%). The DM-DP-treated cuticle had the highest tissue strain at failure (~5.5%), DM-treated slightly lower (~4.5%), and the native cuticle the lowest (~2.5%). The quantified mechanics and statistical significance are shown in Fig. 4(a)-(b). It is noted that the tissue strain and stress changes were mainly from the removal of the mineral phase in cuticle as the mechanical changes were slight when the DM-treated samples were further deproteinized.

3.2.2. Fibrillar-level mechanics along the loading direction

Chitin fibrils along the loading direction show differing elongations in the control, DM and DM-DP groups in response to tensile stress, as may be seen from the corresponding fibril strain-tissue stress curves (Fig. 3b). Again, while the statistical comparison is made in the next subsection, qualitatively we observed that demineralized and demineralized/ partially deproteinized cuticle exhibited larger fibril strain at the same tissue stress alongside a lower increase of tissue stress/fibril strain compared with native cuticle. For example, chitin fibrils from DM- and DM-DP-treated cuticle had a higher extension of ~0.20% compared with native cuticle (~0.13%) at a tissue stress of ~15 MPa.

3.2.3. Macroscale and nanoscale mechanical parameters

The foregoing effects can be made quantitative; macroscopic tissue mechanical parameters changed on chemical treatment, with a reduction in tissue modulus E_T and an increase in the tissue strain at the maximum tensile stress (Fig. 4). The tissue modulus of cuticle decreased significantly ($p < 0.001$, Fig. 4a) by ~80.7% from 3.89 GPa (±0.55) in untreated native cuticle to 0.75 GPa (±0.14) in the DM group. Subsequent change on partial deproteinization reduced the modulus to 0.61 GPa (±0.09), which was a nonsignificant ($p > 0.05$) further reduction when compared to DM group. The demineralization and partial deproteinization treatments produced significant ($p < 0.01$ and $p < 0.001$, respectively) increases in the tissue strain at the maximum stress during tensile testing. The tissue strain in DM group (3.19% ± 0.75) was twice that of untreated native cuticle (1.61% ± 0.73), whilst the tissue strain further increased by around 50%–4.84% (±0.77) in DM-DP group (Fig. 4b).

Similarly, at the fibrillar-level, cuticle showed clear differences in mechanical parameters in chemically modified groups compared with untreated native cuticle. As above, only the fibril strains for fibrils oriented parallel to the loading direction are being considered. The effective fibril modulus ($d\sigma_T/d\varepsilon_F$) [42,43] followed the same decreasing trend as the tissue modulus (Fig. 4c). Compared with the effective fibril modulus ($d\sigma_T/d\varepsilon_F$) in untreated native cuticle (12.37 GPa ± 2.08), chitin fibrils in the DM group exhibited an extremely significant reduction of around 50% (5.64 GPa ± 0.91, $p < 0.001$), while no statistically significant change ($p > 0.05$) was observed when the cuticle was further partially deproteinized (6.51 GPa ± 1.65).

The fraction of the deformation taken up at the fibril level (ratio of fibril strain to tissue strain, $d\varepsilon_F/d\varepsilon_T$) for the native, DM and DM-DP groups (Fig. 4d) also showed a decrease from control to demineralized states (Fig. 4d), with a ratio ($d\varepsilon_F/d\varepsilon_T$) of ~0.22 (±0.06) in the untreated cuticle being larger than that from DM-treated cuticle (~0.13 ± 0.04, $p < 0.01$). The further change of $d\varepsilon_F/d\varepsilon_T$ in DM-DP group, to averaged values of 0.10 (±0.04), was not statistically significant relative to DM.

3.3. Chemical treatment induces non-symmetrical angular fibril strains in the Bouligand layers

The previous section considered the altered tensile response of the chitin fibrils, oriented along the loading direction, in the different chemically treated cuticle (Figs. 3 and 4). However, as cuticle consists of a plywood array of fibres, an angle-dependent anisotropic deformation for off-axis fibres is expected. To better understand how the matrix changes modify the coupled angular deformation of the chitin nanofibrils in this architecture, we investigated the deformation behavior of the chitin fibrils from different sublayers of the Bouligand lamellae when tensile strain was applied.

The fibril strain in chitin fibrils and the inverse effective fibril modulus ($d\varepsilon_F/d\sigma_T$), at angles (χ) from 0° to 90° were calculated from the shifts on the angularly resolved profiles of (002) diffraction (corresponding to different sub-lamellae; Fig. 1c and d). The slope-change of inverse effective fibril modulus ($d\varepsilon_F/d\sigma_T$) with azimuthal angle, averaged across samples in the three groups, are shown in Fig. 5, and the statistical comparison between groups at each angle is shown in Table 2. Plots of the individual fibril-strain vs. tissue stress plots as a function of angle (whose group-averaged gradients are plotted in Fig. 5), are shown in Supplementary Figure S5. From these figures it can be seen that in control-group cuticle, chitin fibrils from differently orientated sub-lamellae exhibited symmetrical response to the stress during stretching, from positive strains (at angles near zero) gradually decreasing to zero strain at ~45–50°, followed by negative strains (Poisson contraction) for larger off-axis up to 90° [28]. In contrast to the symmetrical change with angle seen in native cuticle, for DM- and DM-DP-treated cuticle, extensional stress resulted in elongation of only the chitin fibrils close to the loading direction (~0°–40°), with small compression / non-deformation e chitin fibrils away from the loading direction (~50°–90°). The rate of change of the inverse effective fibril modulus ($d\varepsilon_F/d\sigma_T$), as a function of fibre angle, is

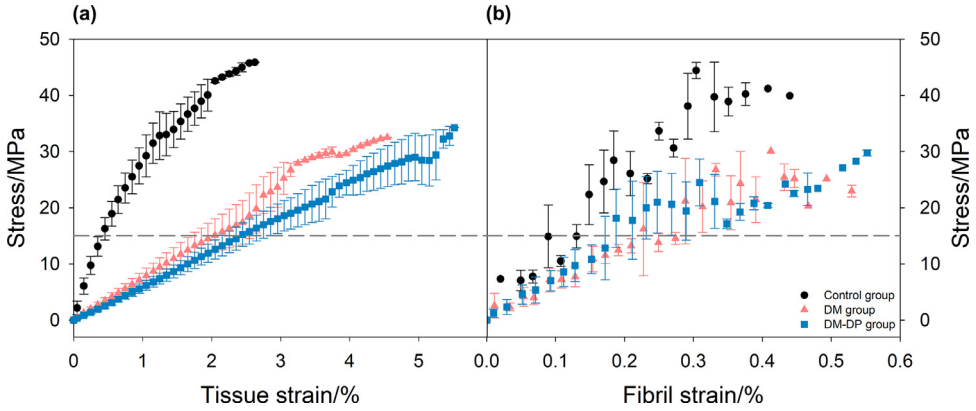

Fig. 3. Demineralization and deproteinization of stomatopod cuticle lead to changes in stress response at macro- and nanoscale. (a) Macroscale stress response in chemical modified cuticle during tensile testing at a rate of 0.05%/s, averaged over multiple samples (control: black, $n = 7$; DM: pink, $n = 7$; and DM-DP: blue, $n = 6$), binned according to tissue strain (bin width: 0.1%), showing difference in strain and modulus. (b) Corresponding fibril strain/tensile stress curves for the control, DM and DM-DP groups, binned with the width of 0.02% fibril strain. Demineralized and demineralized/partially deproteinized cuticle exhibits larger fibril strain in response to tensile stress alongside a lower rate increase of fibril strain compared with control. Errors bars represent standard deviations. (For interpretation of the references to colour in this figure legend, the reader is referred to the web version of this article.)

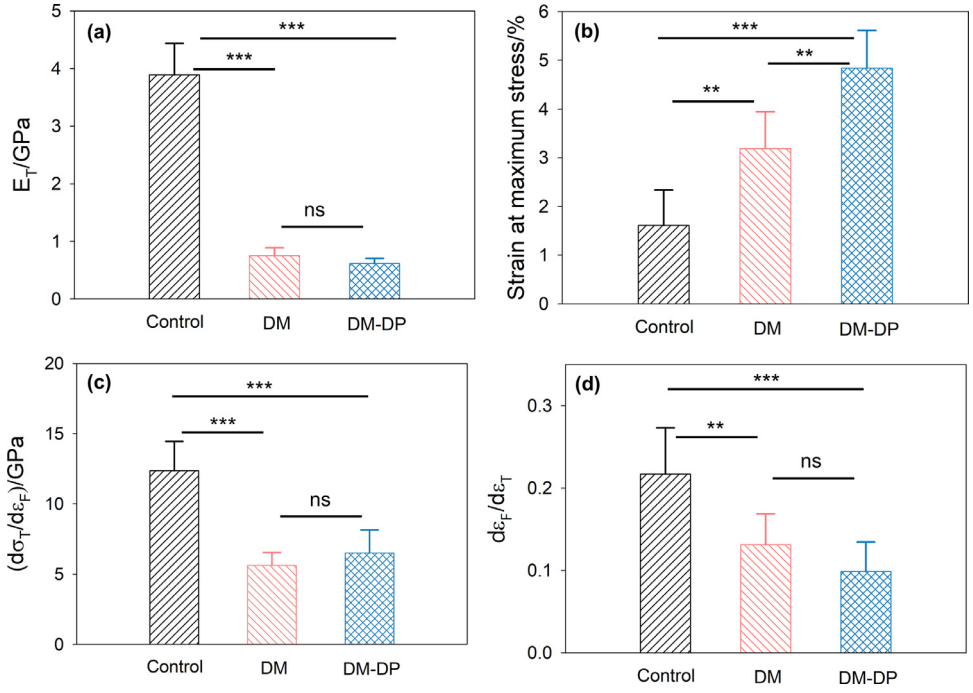

Fig. 4. Quantified tensile mechanics of cuticle before and after chemical modification. (a) Tissue modulus E_T plotted of elastic regions for control (black, $n = 7$), DM (pink, $n = 7$) and DM-DP (blue, $n = 6$) groups. At tissue level, DM- and DM-DP-treated cuticle shows much lower modulus compared with the control group ($p < 0.001$), whereas the modulus change from further deproteinization of the demineralized samples is almost negligible. (b) The cuticle experiences much higher tissue strain in DM- and DM-DP-states compared with the control group. (c) At fibrillar level, chitin fibrils follow the same trend in the tissue stress change rate in response to fibril strain (effective fibril modulus) with the tissue modulus. (d) The fraction of the deformation taken up at the fibril level (ratio of fibril strain to tissue strain) is less for cuticle in DM and DM-DP groups compared with the control group. Error bars represent standard deviations and *'s indicates statistical significance between groups (i.e. *: $p < 0.05$; **: $p < 0.01$; ***: $p < 0.001$; ns: not significant). (For interpretation of the references to colour in this figure legend, the reader is referred to the web version of this article.)

faster in the DM and DM-DP groups compared to controls. The neutral plane (where the slope crosses 0) was around 30° for DM and DM-DP groups, whereas for native cuticle the reduction was more gradual and the neutral plane was around 45°–50°. The slope showed a sharp change from ~0.016% MPa^{-1} to 0 at the azimuthal angle of 30° in DM- and DM-DP-treated groups, in compared with a slow and gradual decrease from ~0.007% MPa^{-1} to 0 at a larger azimuthal angle of 50° in the native cuticle. Differences between the rates across groups are significant for angles toward the loading direction, as can be seen at 0°, 10°, 30°, 40° and 50° in Fig. 5 and Table 2. For angles at 60° and above, there are no significant differences between the groups.

4. Discussion

In summary, from our investigations into the nanoscale mechanics of native, demineralized and demineralized/partially deproteinized cuticle, we find:

- Demonstration of significant relative changes in chitin molecular lattice spacing on demineralization and partial deproteinization (Fig. 2)
- Alterations in fibrillar-deformation mechanisms, fibril strain ratios and effective fibril moduli with the same treatments, with the major change arising upon demineralization (Figs. 3 and 4)

Table 2
For data shown in Fig. 5, differences between the inverse fibril-moduli (across groups) at different angles. *p*-values are reported for 1-way ANOVA tests (column 2); Holm-Sidak pairwise comparison *p*-values are reported if a significant ($p < 0.05$) difference is observed at a specific angle. *'s indicates statistical significance between groups (i.e. *: $p < 0.05$; **: $p < 0.01$; ***: $p < 0.001$; ns: not significant).

Angle	*p* (ANOVA)	*p* (Control vs. DM)	*p* (Control vs. DM-DP)	*p* (DM vs. DM-DP)
0°	<0.001 (***)	<0.001 (***)	<0.001 (***)	0.281 (ns)
10°	0.028 (*)	0.028 (*)	0.390 (ns)	0.137 (ns)
20°	0.755 (ns)	–	–	–
30°	0.002 (**)	0.004 (**)	0.007 (**)	0.862 (ns)
40°	0.003 (**)	0.003 (**)	0.045 (*)	0.159 (ns)
50°	0.017 (*)	0.019 (*)	0.104 (ns)	0.261 (ns)
60°	0.325 (ns)	–	–	–
70°	0.339 (ns)	–	–	–
80°	0.114 (ns)	–	–	–
90°	0.188 (ns)	–	–	–

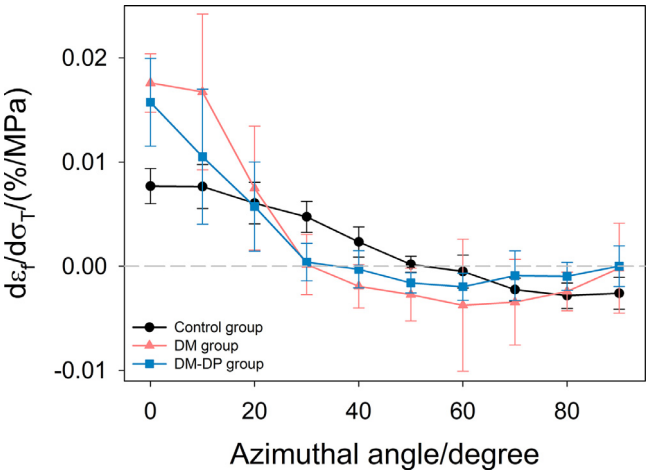

Fig. 5. Inverse effective fibril modulus ($d\varepsilon_f/d\sigma_T$) at different angles to the loading axis, showing the angular variation of tensile stress response of chitin fibrils from differently oriented sub-lamellae (χ from 0° to 90°). The deformation of chitin fibrils changes faster from extension to non-deformation/compression (slope from positive to near-zero/negative) with a neutral plane at around 30° in the DM (pink, $n = 7$) and DM-DP (blue, $n = 6$) groups compared with the gradual change in the control group (neutral plane around 50°, black, $n = 7$). Error bars represent standard deviations. See also Table 2 for statistical analysis. (For interpretation of the references to colour in this figure legend, the reader is referred to the web version of this article.)

- Matrix-digestion induced disruption of an angle-dependent, laminate-type pattern of anisotropic nanoscale deformation in the Bouligand layers (Fig. 5).

In the following, we discuss these findings in turn, in relation to the literature, followed by some discussion of the limitations of the work.

Firstly, the observed increase in axial lattice spacing on demineralization in cuticle may be related to similar effects in biomineralized collagen (e.g. vertebrate bone and dentin), where the axial fibrillar electron density modulation (at the nanometer scale) reduces from 67 nm (unmineralized) to 65 nm (mineralized), which is linked to water replacement by mineral [25,62–64]. We suggest the chitin fibrils may be pre-compressed in the mineralized state, and this pre-strain is lost on demineralization (Fig. 6a-b). On demineralization, water (which adheres to both the chitin and protein phases by H-bonding [37]) will replace the mineral in the hydrated cuticle, and it is possible that hydration induced swelling-pressure (as occurs in cartilage [33]) will contribute to the removal of pre-strain. It has been reported that for mineralized collagen, dehydration led to a 2.5% collagen fibrillar contraction [65] in mineralized tendon and a 0.3% compressive strain in mineral particles in dentin [25], in comparison to the current work where a ~0.10% compressive pre-strain is lost on demineralization. Taking the modulus of the chitin-fibril/protein fibre aggregates as ~22 GPa [66], this corresponds to a stress level of ~22 MPa, suggestive of internal pre-stresses in the tissue. The subsequent partial-deproteinization step changes the lattice spacing to lower values (by ~0.10%). Prior work has proposed that the (010) face of chitin is bonded to a silk-like β-sheet proteins in the insect cuticle [38,39]. As shown in [39], three times the 0.69 nm protein period (2.07 nm) in protein is almost the same (0.3% larger) than twice the *c*-lattice spacing in chitin (2.064 nm) [39], suggesting a stereo-chemical match and strong protein/chitin interactions. Hence, the chitin fibrils will need to be in a pre-tensed state in the DM-group (by 0.3%) to maximize the interaction with the attached protein, as well as due to swelling pressure from a stabilized water phase. We speculate that partial deproteinization (to the DM-DP group) may reduce this pre-tension, resulting in the observed reduction of chitin (002)-lattice spacing by 0.10% upon partial deproteinization. A schematic of the different constituents of the cuticle nanostructure in the control-, DM- and DM-DP-states, and their interaction, is shown in Fig. 6.

Secondly, our *in situ* experimental results demonstrate clear alterations in the deformation mechanisms in cuticle at both tissue and fibrillar levels upon chemical modification of the matrix. At the macroscale, the values of tissue moduli obtained (~3.3–4.4 GPa) are in the same range as prior work on lobster cuticle [67]. The significant reduction in tissue modulus (~80%) and increase in tissue strain (~200–300%) in the chemical treated (DM and DM-DP) cuticle compared to the controls (Figs. 4a and b) is higher than the difference in mechanical properties of lobster cuticle from dry to hydrated state (~30%) [67]. At the nanoscale, there is little prior experimental data on the fibrillar-level deformations in cuticle. X-ray diffraction was used to estimate individual chitin nanofibril moduli (from snow crab tendons) at ~60 – 120 GPa [55,68], although it is noted that in [55], the chitin nanofibril modulus was calculated by dividing macroscopic stress by percentage change in the (004) lattice spacing – i.e. macroscopic stress was taken to be the same as nanoscale stress on individual chitin fibrils. From modelling studies, the chitin-fibril/protein nanofibres (aggregates of fibrils) in lobster cuticle have been proposed to have moduli of ~22 GPa versus ~12 GPa for the mineral-protein matrix [66]). The measurements of fibril strain reported here are the average fibril strain in the chitin-fibril/protein nanofibres. From our results, the fibril-to-tissue strain ratio ~0.2 in the native cuticle (Fig. 4d) and the numerical value being < 1 indicate that the fibril strain was a fraction of the total strain and some amount of shearing strain is carried by the matrix, as also found in other mineralized fibrous nanocomposites [28,54]. From the fibril-to-tissue strain-ratios, inferences on the changes in interfibrillar matrix mechanical properties can also be made. Staggered models of nanofibres in an interfibrillar matrix [56,69–71] have been used earlier to predict the elastic modulus of biological tissues like bone and tendon,

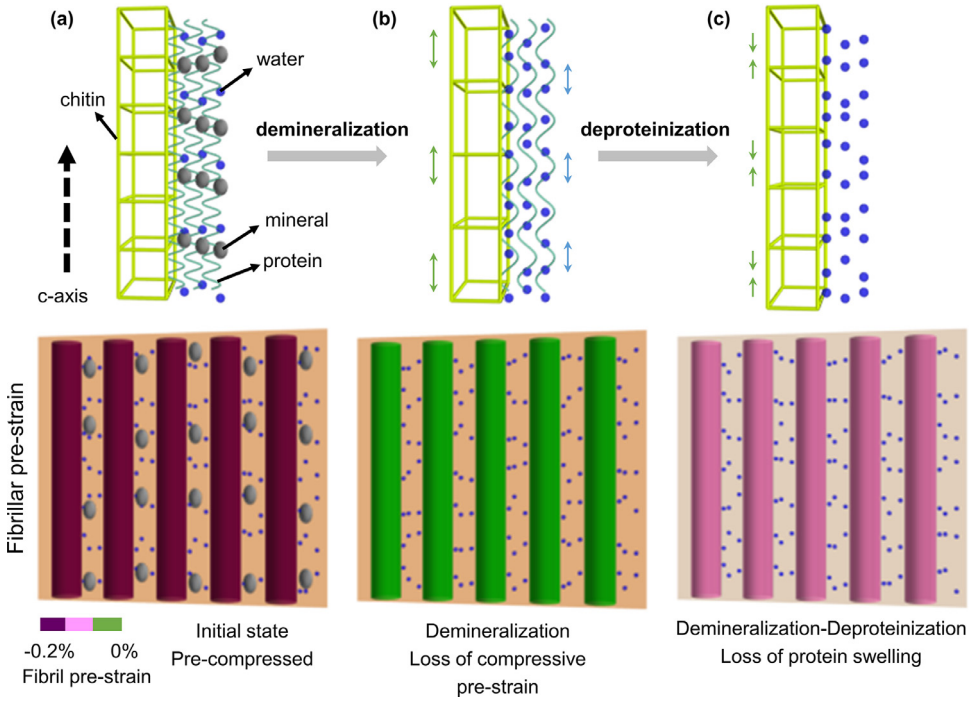

Fig. 6. Schematic of the cuticle composite under different chemical treatments, where chitin interacts with the mineral particles and proteins in the hydrated state. (a) In the native cuticle, at the molecular scale (upper), the chitin crystals (cuboid, the lattice spacing $D_{(002)}$ along *c*-axis is shown by arrows) is stabilized by the mineral particles (grey ellipsoids) with the presence of protein (wavy lines) and water molecules (blue spheres), while at the fibre level (lower), the chitin fibres (straight lines: strained in dark red) are in a state of compressive prestrain due to the interaction with the mineralized matrix (brown). (b) In the demineralized cuticle, the mineral particles are removed and replaced with water, the compressive pre-strain is lost (lower, non-strained in green), swelling pressure increased due to hydrated proteins (indicated by the blue arrows, upper), and the chitin lattice spacing $D_{(002)}$ increases (indicated by the green arrows, upper). (c) After further partial deproteinization of the demineralized cuticle, much of the protein is removed, and the bonding of the protein molecules with chitin and associated swelling pressure is also reduced, leading to a reduction in lattice spacing $D_{(002)}$ (indicated by the green arrows, upper) in chitin. (For interpretation of the references to colour in this figure legend, the reader is referred to the web version of this article.)

although the model is a considerable simplification by considering the tissue to be only parallel fibred. In this model, the elastic modulus of the tissue E_T is related to the modulus of the fibril E_F, extrafibrillar matrix E_M, fibril volume fraction ϕ and aspect ratio of the fibrils ρ as:

$$E_T = E_F\phi\left(1+\frac{4}{\rho^2}\frac{1-\phi}{\phi}\frac{E_F}{\gamma E_M}\right)^{-1} + E_M(1-\phi) \quad (1)$$

The ratio of the tissue strain to fibril strain is:

$$\frac{\varepsilon_T}{\varepsilon_F} = 1+\frac{4}{\rho^2}\frac{1-\phi}{\phi}\frac{E_F}{\gamma E_M} \quad (2)$$

From the above equations, it is seen that as the matrix modulus E_M reduces, both the ratio $\varepsilon_F/\varepsilon_T$ and tissue modulus E_T will decrease (for a constant strain-rate test in the elastic range, $\varepsilon_F/\varepsilon_T$ and $d\varepsilon_F/d\varepsilon_T$ are equivalent). Here we assume that the chemical modification protocol (DM and DM-DP) affects mainly the matrix between the fibres (demineralization and then partial deproteinization), hence the modulus of the chitin/protein fibres E_F is taken as constant. From Fig. 4d, the left-hand side of (2) is approximately 5 (control) and 10 (DM- and DM-DP). From this, the ratio of matrix moduli in DM- (or DM-DP-) to control-cases is approximately 0.44. However, this ratio is larger than expected from earlier multiscale simulation results on lobster cuticle, where amorphous calcium carbonate moduli of E_m ~37 GPa [68,72] and protein moduli of E_p ~1 GPa [66,68,73]) are obtained. In lobster cuticle [73], protein volume fraction in the matrix and in the chitin/protein fibres has been estimated at 0.10 and 0.69, respectively, and the volume fraction of the fibres at 0.22. From this, an overall protein volume fraction of ~0.23 and mineralized matrix modulus of 33.4 GPa is obtained, leading to a ratio of matrix moduli after and before demineralization as ~0.03. We believe the main reason for this discrepancy is because we have used a parallel fibred model to represent the cuticle, whereas the simulations in [68] used ply-laminate theory and homogenisation procedures for a more realistic multiscale model. Comparing our experimental predictions to these more complex models could be an area for future work. A secondary reason for this discrepancy may lie in the fact that shear moduli of nano-confined layers of biopolymer matrices may be larger than bulk measurements. It is noted that the strain-ratio does not further reduce significantly for the DM-DP group – possibly indicating that mineral is the main critical component determining the tensile properties of the cuticle matrix (and the tissue mechanics). From the staggered model formulae, it can also be observed that a reduction in matrix modulus will result in a larger fibril strain at the same overall tissue stress.

Thirdly, the alteration in the angular-dependent deformation of the chitin fibrils in the DM and DM-DP groups, relative to control, is evidence that the treatments decouple the layers of the laminate and change the stress-transfer pathways. In native cuticle, the tensile deformation along the loading direction changing to compression in the perpendicular fibres (Poisson effect; Fig. 5a) implies a strong interconnection between the fibrils in different sub-lamellae in the Bouligand arrangement. These interconnections include the transversely-running pore-canal fibres mechanically interlocking the fibrous network [28,68], and the matrix/fibre adhesion. When chemically modified (DM and DM-DP), the fibre-matrix adhesion is weakened at the interface and less efficient loading transfer between fibres, and between the lamellar layers.

The values of (002) chitin lattice spacing observed in this work can be compared to prior work [12,46,74], on fly-ovipositor, spider-fang, and lobster carapace. Summarizing this, Table 3 shows that the range of the (002) lattice spacing in tergite cuticle reported here (~0.513 – 0.514 nm) are lower than the values for spider leg

Table 3
Chitin *c*-axis (002) lattice spacing from prior WAXD measurements (including chemically modified cuticle) and the current study. Figures in italics in last three rows are diffraction-geometry corrected values (see Discussion in main text for details).

Sample	$D_{(002)}$ /nm	References
Chitin from lobster	0.516 ± 0.001	Minke and Blackwell [46]
Lobster carapace	0.51	Erko, Hartmann et al. [74]
Spider fang	0.51	Erko, Hartmann et al. [74]
Spider leg (intact wet)	0.5155 ± 0.0025	Serrano, Leemreize et al. [12]
Spider leg (partly deproteinized wet)	0.5175 ± 0.0065	Serrano, Leemreize et al. [12]
Spider leg (Bleached wet)	0.516 ± 0.0005	Serrano, Leemreize et al. [12]
Stomatopod (Mantis shrimp) cuticle (control)	0.5131 ± 0.0003(*0.5150 ± 0.0003*)	This study
Stomatopod (Mantis shrimp) cuticle (DM)	0.5136 ± 0.0004(*0.5155 ± 0.0004*)	This study
Stomatopod (Mantis shrimp) cuticle (DM-DP)	0.5131 ± 0.0002(*0.5150 ± 0.0002*)	This study

(~0.516 – 0.518 nm [12]) and chitin from lobster (~0.516 nm [46]). Modelling data on lobster cuticle predict 5.225 Å [68]. Interestingly, however, our work on tergite cuticle shows that the measured (002) lattice spacing is slightly different depending on the orientation in which the cuticle plane is placed with respect to the beam, and here we discuss this effect in light of the above lower values. Specifically, all measurements here are for the beam normal to the surface of the cuticle (denoted by us as L1-geometry earlier [28]). An alternate (L2-) orientation is perpendicular to the thickness of the cuticle (which also enables us to measure the exo- and endocuticle regions separately). Our finding is that (002) peak positons for tergite are ~0.516–0.517 nm for L2 (on average; Supplementary Fig. S6) versus the ~0.513–0.514 nm in L1-orientation. To explain this difference, diffraction-geometry effects need to be considered (Supplementary Figure S7). As shown in Supplementary Fig. S7 (C)-(D), for a single fibre orthogonal to the beam, the (002) peak is only visible because a) the angle is small and b) the finite width of the (002) reciprocal space intensity ellipsoid along the beam-direction means that the tails of the ellipsoidal distribution intersect the Ewald sphere. In L1-geometry, the (002) intensity distribution in reciprocal space for a Bouligand plywood distribution is a narrow band of intensity, arising from convolving the ellipsoid with a uniform angular distribution, and the measured (002) peak position along the vertical slice will be arising from the intersection mentioned above. In L2-geometry, however, the band is rotated by 90°, and intersects the Ewald sphere. The apparent scattering wavevector arising from the intersection of the tail of the ellipsoidal intensity distribution (L1) is slightly larger than the real wavevector arising when the center of the distribution intersects the Ewald sphere (L2). It can be shown that (Supplementary Figure S7 and text following) $d_{app} = \lambda/(2\ \sin((\arcsin(\lambda/d))/2))$ where λ is the X-ray wavelength used (note that the value reduces to d for the small-angle scattering case of $\lambda \rightarrow 0$, as expected). For the X-ray energy used, this value is d_{app}=0.514 nm when $d = 0.516$ nm, closer to our results. To facilitate comparison in the Supplementary Table S2, we have added the corrected d value in parentheses below our measured values. Note that all samples in the current study (control, DM and DM-DP) are in the L1-geometry only, and as we are interested in relative rather than absolute changes between the groups, this effect does not change our conclusions.

Concerning the limitations of our work, we can identify the following main areas. Firstly, the deproteinization protocol may remove only part of the total proteins, because our samples are in the form of solid slices, not the powder version used in [51], as sections are needed for *in situ* mechanical testing of the cuticle close to its native state. Mushi et al. found, in lobster exoskeleton powder, a residual protein content ~4.7% after 20% NaOH treatment for two weeks [51]. In our treatment, using the same protocol, the samples are bulk instead of powder and more protein is likely to have remained. To partly mitigate this, we sectioned the samples into relatively thin slices, so that the exo- and endocuticle surfaces are open to media inflow (rather than using intact shells with inflow through the top (epicuticle) and bottom surfaces). However, the use of quantitative probes of the chemical composition (e.g. Raman spectroscopy) would be useful to determine the amount of protein loss. Secondly, our X-ray diffraction measurements provide an averaged signal across both exo- and endocuticle in L1-geometry. As a result, relative differences in the matrix-modification protocol in the two regions are not detected. Testing in L2-geometry would enable the beam to focus on the exo- and endocuticle separately, but from our experience of testing in this orientation, small sample lateral motion (of the order of a few microns) occurs during axial stretching, and may cause loss of spatial resolution. Possibly, a combination of X-ray diffraction with full-field imaging methods like tomography would be useful to circumvent this problem. Thirdly, we did not explicitly consider 3D fibrillar reorientation under loading; our prior work shows that small, load-induced changes in sample angles occur and can significantly alter the angular intensity distribution (Supplementary Fig. S3 and [28]). To obtain estimates of these effects, texture (sample rotation) or use of novel energy-dispersive [75] or tensor tomography methods [76] proposed recently may be necessary. Fourthly, our analysis uses only X-ray diffraction to analyze ultrastructural changes; alterations in the local chemical environment are not detected, and combining the X-ray analysis with infra-red or Raman spectroscopy may be useful in providing a closer insight into the processes at the fibrillar- and molecular level.

5. Conclusion

In summary, we have used *in situ* synchrotron X-ray diffraction to reveal how the ultrastructural architecture and mechanics of α-chitin fibrillar networks in arthropod cuticle depend on the interactions between the nanoscale components: fibrillar chitin, non-fibrillar proteins, and inorganic calcium carbonate minerals. By measuring the crystallographic lattice spacing of the α-chitin crystal structure (specifically, the (002) peak), we find a significant increase in $D_{(002)}$ in demineralized cuticle compared to native cuticle, followed by a significant decrease in partially-deproteinized tissue compared to the demineralized cuticle. These lattice spacing changes may imply i) a compressive pre-strain in chitin fibres, induced by stabilization of mineral particles, which is lost on demineralization and associated hydration, and ii) a swelling-pressure induced tensile pre-strain of chitin fibres by the protein-phase. We find altered fibrillar deformation mechanics on demineralization and deproteinization – increased fibrillar flexibility and reduced fibril/tissue strain ratio combined with decreased macroscale tissue stiffness. A simplified model suggests these effects arise due to the modification of the mineral/protein matrix properties, which transfers loads between fibrils by shearing. At one scale higher (microstructural level), significant alterations in the angular-dependent strain and stresses in the plywood lamellae, possibly due to weakening of the interaction and bonding between fibres in adjacent lamellae. While the biochemical details

of interactions between chitin fibrils and other phases (mineral, protein, and water) in cuticle need further elucidation, we suggest these changes in crystal structure and mechanisms – at the mesoscopic or nanoscale level – will shed light on understanding chitin nanomechanics, which is of fundamental importance in both the biomechanics of arthropod cuticle and other mineralized tissues, as well as in design of new bio-inspired chitin-based materials [3, 9].

Declaration of Competing Interest

The authors declare that they have no known competing financial interests or personal relationships that could have appeared to influence the work reported in this paper.

Acknowledgements

Yanhong Wang is supported by the China Scholarship Council (CSC). We thank Diamond Light Source (Harwell, UK) for the generous award of synchrotron beamtime (SM17869), and Dr. Andrew J. Smith, Dr... Tim Snow and Dr.... Olga Shebanova for excellent technical support during the beamtime. Nicholas J. Terrill thanks the BBSRC (BB/R004773/1) for research grant funding. Ettore Barbieri is supported by JSPS KAKENHI Grant Number JP18K18065 and the Cross-Ministerial Strategic Innovation Promotion (SIP) Program for Deep Ocean Resources. Nicola M. Pugno is supported by the European Commission with the Graphene Flagship Core 2 n. 785219 (WP14 “Composites”) and FET Proactive “Neurofibres” n. 732344 as well as by the MIUR with the “Departments of Excellence” grant L. 232/2016, ARS01-01384-PROSCAN and PRIN-20177TTP3S. Himadri S. Gupta thanks the BBSRC (BB/R003610/1) and UKRI (MR/R025673/1) for research grant funding.

Supplementary materials

Supplementary material associated with this article can be found, in the online version, at doi:10.1016/j.actbio.2019.09.036.

References

[1] R. Weinkamer, P. Fratzl, Mechanical adaptation of biological materials - the examples of bone and wood, Mat. Sci. Eng. C-Mater. 31 (6) (2011) 1164–1173.
[2] P. Egan, R. Sinko, P.R. LeDuc, S. Keten, The role of mechanics in biological and bio-inspired systems, Nat. Commun. 6 (2015) 7418.
[3] S.E. Naleway, M.M. Porter, J. McKittrick, M.A. Meyers, Structural design elements in biological materials: application to bioinspiration, Adv. Mater. 27 (37) (2015) 5455–5476.
[4] M.A. Meyers, P.Y. Chen, A.Y.M. Lin, Y. Seki, Biological materials: structure and mechanical properties, Prog. Mater. Sci. 53 (1) (2008) 1–206.
[5] H. Ehrlich, D. Janussen, P. Simon, V.V. Bazhenov, N.P. Shapkin, C. Erler, M. Mertig, R. Born, S. Heinemann, T. Hanke, H. Worch, J.N. Vournakis, Nanostructural organization of naturally occurring composites - Part II: silica-chitin-based biocomposites, J. Nanomater. (2008) 54.
[6] Y. Yang, Z.Y. Chen, X. Song, Z.F. Zhang, J. Zhang, K.K. Shung, Q.F. Zhou, Y. Chen, Biomimetic anisotropic reinforcement architectures by electrically assisted nanocomposite 3D printing, Adv. Mater. 29 (11) (2017) 1605750.
[7] P.Y. Chen, J. McKittrick, M.A. Meyers, Biological materials: functional adaptations and bioinspired designs, Prog. Mater. Sci. 57 (8) (2012) 1492–1704.
[8] L.K. Grunenfelder, G. Milliron, S. Herrera, I. Gallana, N. Yaraghi, N. Hughes, K. Evans-Lutterodt, P. Zavattieri, D. Kisailus, Ecologically driven ultrastructural and hydrodynamic designs in stomatopod cuticles, Adv. Mater. 30 (9) (2018) 1705295.
[9] Z.Q. Liu, M.A. Meyers, Z.F. Zhang, R.O. Ritchie, Functional gradients and heterogeneities in biological materials: design principles, functions, and bioinspired applications, Prog. Mater. Sci. 88 (2017) 467–498.
[10] A. Herman, L. Addadi, S. Weiner, Interactions of sea-urchin skeleton macromolecules with growing calcite crystals—a study of intracrystalline proteins, Nature 331 (6156) (1988) 546.
[11] A. Berman, L. Addadi, Å. Kvick, L. Leiserowitz, M. Nelson, S. Weiner, Intercalation of sea urchin proteins in calcite: study of a crystalline composite material, Science 250 (4981) (1990) 664–667.
[12] C.V. Serrano, H. Leemreize, B. Bar-On, F.G. Barth, P. Fratzl, E. Zolotoyabko, Y. Politi, Ordering of protein and water molecules at their interfaces with chitin nano-crystals, J. Struct. Biol. 193 (2) (2016) 124–131.
[13] H.O. Fabritius, A. Ziegler, M. Friak, S. Nikolov, J. Huber, B.H.M. Seidl, S. Ruangchai, F.I. Alagboso, S. Karsten, J. Lu, A.M. Janus, M. Petrov, L.F. Zhu, P. Hemzalova, S. Hild, D. Raabe, J. Neugebauer, Functional adaptation of crustacean exoskeletal elements through structural and compositional diversity: a combined experimental and theoretical study, Bioinspir. Biomim. 11 (5) (2016) 055006.
[14] P. Romano, H. Fabritius, D. Raabe, The exoskeleton of the lobster Homarus americanus as an example of a smart anisotropic biological material, Acta Biomater. 3 (3) (2007) 301–309.
[15] H.O. Fabritius, C. Sachs, P.R. Triguero, D. Raabe, Influence of structural principles on the mechanics of a biological fiber-based composite material with hierarchical organization: the exoskeleton of the lobster Homarus Americanus, Adv. Mater. 21 (4) (2009) 391–400.
[16] J.C. Weaver, G.W. Milliron, A. Miserez, K. Evans-Lutterodt, S. Herrera, I. Gallana, W.J. Mershon, B. Swanson, P. Zavattieri, E. DiMasi, D. Kisailus, The stomatopod dactyl club: a formidable damage-tolerant biological hammer, Science 336 (6086) (2012) 1275–1280.
[17] A. Al-Sawalmih, C.H. Li, S. Siegel, H. Fabritius, S.B. Yi, D. Raabe, P. Fratzl, O. Paris, Microtexture and chitin/calcite orientation relationship in the mineralized exoskeleton of the American Lobster, Adv. Funct. Mater. 18 (20) (2008) 3307–3314.
[18] L. Addadi, S. Raz, S. Weiner, Taking advantage of disorder: amorphous calcium carbonate and its roles in biomineralization, Adv. Mater. 15 (12) (2003) 959–970.
[19] F. Neues, A. Ziegler, M. Epple, The composition of the mineralized cuticle in marine and terrestrial isopods: a comparative study, CrystEngComm 9 (12) (2007) 1245–1251.
[20] F. Bobelmann, P. Romano, H. Fabritius, D. Raabe, M. Epple, The composition of the exoskeleton of two crustacea: the American lobster Homarus americanus and the edible crab cancer Pagurus, Thermochim. Acta 463 (1–2) (2007) 65–68.
[21] Y. Bouligand, Twisted fibrous arrangements in biological-materials and Cholesteric mesophases, Tissue Cell 4 (2) (1972) 189–217.
[22] D. Raabe, P. Romano, C. Sachs, A. Al-Sawalmih, H.-.G. Brokmeier, S.-.B. Yi, G. Servos, H. Hartwig, Discovery of a honeycomb structure in the twisted plywood patterns of fibrous biological nanocomposite tissue, J. Cryst. Growth 283 (1) (2005) 1–7.
[23] P. Fratzl, H.S. Gupta, E.P. Paschalis, P. Roschger, Structure and mechanical quality of the collagen-mineral nano-composite in bone, J. Mater. Chem. 14 (14) (2004) 2115–2123.
[24] H.S. Gupta, W. Wagermaier, G.A. Zickler, D.R.B. Aroush, S.S. Funari, P. Roschger, H.D. Wagner, P. Fratzl, Nanoscale deformation mechanisms in bone, Nano Lett. 5 (10) (2005) 2108–2111.
[25] J.B. Forien, I. Zizak, C. Fleck, A. Petersen, P. Fratzl, E. Zolotoyabko, P. Zaslansky, Water-Mediated collagen and mineral nanoparticle interactions guide functional deformation of human tooth dentin, Chem. Mater. 28 (10) (2016) 3416–3427.
[26] M. Tadayon, S. Amini, A. Masic, A. Miserez, The Mantis Shrimp saddle: a biological spring combining stiffness and flexibility, Adv. Funct. Mater. 25 (41) (2015) 6437–6447.
[27] Y. Zhang, O. Paris, N.J. Terrill, H.S. Gupta, Uncovering three-dimensional gradients in fibrillar orientation in an impact-resistant biological armour, Sci. Rep. 6 (2016) 26249.
[28] Y. Zhang, P. de Falco, Y. Wang, E. Barbieri, O. Paris, N.J. Terrill, G. Falkenberg, N. Pugno, H.S. Gupta, Towards in situ determination of 3D strain and reorientation in the interpenetrating nanofibre networks of cuticle, Nanoscale 9 (31) (2017) 11249–11260.
[29] S. Amini, A. Masic, L. Bertinetti, J.S. Teguh, J.S. Herrin, X. Zhu, H.B. Su, A. Miserez, Textured fluorapatite bonded to calcium sulphate strengthen stomatopod raptorial appendages, Nat. Commun. 5 (2014) 3187.
[30] J.R.A. Taylor, S.N. Patek, Ritualized fighting and biological armor: the impact mechanics of the mantis shrimp's telson, J. Exp. Biol. 213 (20) (2010) 3496–3504.
[31] Y.P. Tan, S. Hoon, P.A. Guerette, W. Wei, A. Ghadban, C. Hao, A. Miserez, J.H. Waite, Infiltration of chitin by protein coacervates defines the squid beak mechanical gradient, Nat. Chem. Biol. 11 (7) (2015) 488–495.
[32] A. Miserez, T. Schneberk, C.J. Sun, F.W. Zok, J.H. Waite, The transition from stiff to compliant materials in squid beaks, Science 319 (5871) (2008) 1816–1819.
[33] S.R. Inamdar, D.P. Knight, N.J. Terril, A. Karunaratne, F. Cacho-Nerin, M.M. Knight, H.S. Gupta, The secret life of collagen: temporal changes in nanoscale fibrillar pre-strain and molecular organization during physiological loading of cartilage, ACS Nano. 11 (10) (2017) 9728–9737.
[34] J.E. Rebers, J.H. Willis, A conserved domain in arthropod cuticular proteins binds chitin, Insect Biochem. Mol. 31 (11) (2001) 1083–1093.
[35] A. Miserez, D. Rubin, J.H. Waite, Cross-linking chemistry of Squid Beak, J. Biol. Chem. 285 (49) (2010) 38115–38124.
[36] Z.C. Yu, D. Lau, Molecular dynamics study on stiffness and ductility in chitin-protein composite, J. Mater. Sci. 50 (21) (2015) 7149–7157.
[37] K. Jin, X. Feng, Z. Xu, Mechanical properties of chitin–protein interfaces: a molecular dynamics study, Bionanoscience 3 (3) (2013) 312–320.
[38] J. Blackwell, M.A. Weih, Structure of chitin-protein complexes - Ovipositor of the Ichneumon fly Megarhyssa, J. Mol. Biol. 137 (1) (1980) 49–60.
[39] J.F.V. Vincent, U.G.K. Wegst, Design and mechanical properties of insect cuticle, Arthropod Struct. Dev. 33 (3) (2004) 187–199.

[40] B. Pokroy, A.N. Fitch, E. Zolotoyabko, The microstructure of biogenic calcite: a view by high-resolution synchrotron powder diffraction, Adv. Mater. 18 (18) (2006) 2363–2368.
[41] L. Bertinetti, A. Masic, R. Schuetz, A. Barbetta, B. Seidt, W. Wagermaier, P. Fratzl, Osmotically driven tensile stress in collagen-based mineralized tissues, J. Mech. Behav. Biomed. 52 (2015) 14–21.
[42] L. Xi, P. De Falco, E. Barbieri, A. Karunaratne, L. Bentley, C.T. Esapa, N.J. Terrill, S.D.M. Brown, R.D. Cox, G.R. Davis, N.M. Pugno, R.V. Thakker, H.S. Gupta, Bone matrix development in steroid-induced osteoporosis is associated with a consistently reduced fibrillar stiffness linked to altered bone mineral quality, Acta Biomater. 76 (2018) 295–307.
[43] A. Karunaratne, L. Xi, L. Bentley, D. Sykes, A. Boyde, C.T. Esapa, N.J. Terrill, S.D.M. Brown, R.D. Cox, R.V. Thakker, H.S. Gupta, Multiscale alterations in bone matrix quality increased fragility in steroid induced osteoporosis, Bone 84 (2016) 15–24.
[44] C. Sachs, H. Fabritius, D. Raabe, Hardness and elastic properties of dehydrated cuticle from the lobster homarus americanus obtained by nanoindentation, J. Mater. Res. 21 (8) (2006) 1987–1995.
[45] D. Raabe, C. Sachs, P. Romano, The crustacean exoskeleton as an example of a structurally and mechanically graded biological nanocomposite material, Acta Mater. 53 (15) (2005) 4281–4292.
[46] R. Minke, J. Blackwell, The structure of alpha-chitin, J. Mol. Biol. 120 (2) (1978) 167–181.
[47] P. Sikorski, R. Hori, M. Wada, Revisit of α-Chitin crystal structure using high resolution X-ray diffraction data, Biomacromolecules 10 (5) (2009) 1100–1105.
[48] A. Percot, C. Viton, A. Domard, Optimization of chitin extraction from Shrimp shells, Biomacromolecules 4 (1) (2003) 12–18.
[49] S. Ifuku, M. Nogi, K. Abe, M. Yoshioka, M. Morimoto, H. Saimoto, H. Yano, Simple preparation method of chitin nanofibers with a uniform width of 10–20 nm from prawn shell under neutral conditions, Carbohydr. Polym. 84 (2) (2011) 762–764.
[50] S. Ifuku, M. Nogi, K. Abe, M. Yoshioka, M. Morimoto, H. Saimoto, H. Yano, Preparation of chitin nanofibers with a uniform width as alpha-chitin from crab shells, Biomacromolecules 10 (6) (2009) 1584–1588.
[51] N.E. Mushi, N. Butchosa, M. Salajkova, Q. Zhou, L.A. Berglund, Nanostructured membranes based on native chitin nanofibers prepared by mild process, Carbohydr. Polym. 112 (2014) 255–263.
[52] J. Mo, S.F. Prevost, L.M. Blowes, M. Egertova, N.J. Terrill, W. Wang, M.R. Elphick, H.S. Gupta, Interfibrillar stiffening of echinoderm mutable collagenous tissue demonstrated at the nanoscale, Proc. Natl. Acad. Sci. USA 113 (42) (2016) E6362–E6371.
[53] G. Benecke, M. Kerschnitzki, P. Fratzl, H.S. Gupta, Digital image correlation shows localized deformation bands in inelastic loading of fibrolamellar bone, J. Mater. Res. 24 (2009) 421–426.
[54] H.S. Gupta, J. Seto, W. Wagermaier, P. Zaslansky, P. Boesecke, P. Fratzl, Cooperative deformation of mineral and collagen in bone at the nanoscale, Proc. Natl. Acad. Sci. USA 103 (47) (2006) 17741–17746.
[55] Y. Ogawa, R. Hori, U.J. Kim, M. Wada, Elastic modulus in the crystalline region and the thermal expansion coefficients of alpha-chitin determined using synchrotron radiated X-ray diffraction, Carbohydr. Polym. 83 (3) (2011) 1213–1217.
[56] H. Gupta, S. Krauss, M. Kerschnitzki, A. Karunaratne, J. Dunlop, A. Barber, P. Boesecke, S. Funari, P. Fratzl, Intrafibrillar plasticity through mineral/collagen sliding is the dominant mechanism for the extreme toughness of antler bone, J. Mech. Behav. Biomed. 28 (2013) 366–382.
[57] H.R.C. Screen, J. Seto, S. Krauss, P. Boesecke, H.S. Gupta, Extrafibrillar diffusion and intrafibrillar swelling at the nanoscale are associated with stress relaxation in the soft collagenous matrix tissue of tendons, Soft Matter 7 (23) (2011) 11243–11251.
[58] S.R. Stock, J.D. Almer, Strains in bone and tooth via high energy X-ray scattering, Bone 44 (2) (2009) S270 -S270.
[59] J. Filik, A.W. Ashton, P.C.Y. Chang, P.A. Chater, S.J. Day, M. Drakopoulos, M.W. Gerring, M.L. Hart, O.V. Magdysyuk, S. Michalik, A. Smith, C.C. Tang, N.J. Terrill, M.T. Wharmby, H. Wilhelm, Processing two-dimensional X-ray diffraction and small-angle scattering data in dawn 2, J. Appl. Crystallogr. 50 (2017) 959–966.
[60] M. Basham, J. Filik, M.T. Wharmby, P.C.Y. Chang, B. El Kassaby, M. Gerring, J. Aishima, K. Levik, B.C.A. Pulford, I. Sikharulidze, D. Sneddon, M. Webber, S.S. Dhesi, F. Maccherozzi, O. Svensson, S. Brockhauser, G. Naray, A.W. Ashton, Data analysis workbench (DAWN), J. Synchrotron. Radiat. 22 (2015) 853–858.
[61] M. Newville, T. Stensitzki, D. Allen, A. Ingargiola, LMFIT: non-linear least-square minimization and curve-fitting for python, doi:10.5281/zenodo.11813, 2014.
[62] S. Lees, L.C. Bonar, H.A. Mook, A study of dense mineralized tissue by neutron-diffraction, Int. J. Biol. Macromol. 6 (6) (1984) 321–326.
[63] S. Lees, Considerations regarding the structure of the mammalian mineralized osteoid from viewpoint of the generalized packing model, Connect Tissue Res. 16 (4) (1987) 281–303.
[64] P. Fratzl, N. Fratzl-Zelman, K. Klaushofer, Collagen packing and mineralization: an x-ray scattering investigation of turkey leg tendon, Biophys. Soc. 64 (1993) 260–266.
[65] A. Masic, L. Bertinetti, R. Schuetz, S.W. Chang, T.H. Metzger, M.J. Buehler, P. Fratzl, Osmotic pressure induced tensile forces in tendon collagen, Nat. Commun. 6 (2015) 5942.
[66] S. Nikolov, H. Fabritius, M. Petrov, M. Friak, L. Lymperakis, C. Sachs, D. Raabe, J. Neugebauer, Robustness and optimal use of design principles of arthropod exoskeletons studied by ab initio-based multiscale simulations, J. Mech. Behav. Biomed. 4 (2) (2011) 129–145.
[67] C. Sachs, H. Fabritius, D. Raabe, Experimental investigation of the elastic-plastic deformation of mineralized lobster cuticle by digital image correlation, J. Struct. Biol. 155 (3) (2006) 409–425.
[68] S. Nikolov, M. Petrov, L. Lymperakis, M. Friak, C. Sachs, H.O. Fabritius, D. Raabe, J. Neugebauer, Revealing the design principles of high-performance biological composites using ab initio and multiscale simulations: the example of lobster cuticle, Adv. Mater. 22 (4) (2010) 519–526.
[69] S.P. Kotha, S. Kotha, N. Guzelsu, A shear-lag model to account for interaction effects between inclusions in composites reinforced with rectangular platelets, Compos. Sci. Technol. 60 (11) (2000) 2147–2158.
[70] B. Bar-On, H.D. Wagner, Mechanical model for staggered bio-structure, J. Mech. Phys. Solids 59 (9) (2011) 1685–1701.
[71] B.H. Ji, H.J. Gao, Mechanical properties of nanostructure of biological materials, J. Mech. Phys. Solids 52 (9) (2004) 1963–1990.
[72] M. Faatz, W. Cheng, G. Wegner, G. Fytas, R.S. Penciu, E.N. Economou, Mechanical strength of amorphous $CaCo_3$ colloidal spheres, Langmuir 21 (15) (2005) 6666–6668.
[73] S. Nikolov, H. Fabritius, M. Friak, D. Raabe, Integrated multiscale modeling approach for hierarchical biological nanocomposites applied to lobster cuticle, Bulg. Chem. Commun. 47 (2015) 424–433.
[74] M. Erko, M.A. Hartmann, I. Zlotnikov, C. Valverde Serrano, P. Fratzl, Y. Politi, Structural and mechanical properties of the arthropod cuticle: comparison between the fang of the spider Cupiennius salei and the carapace of American lobster Homarus americanus, J. Struct. Biol. 183 (2) (2013) 172–179.
[75] T.A. Grünewald, H. Rennhofer, P. Tack, J. Garrevoet, D. Wermeille, P. Thompson, W. Bras, L. Vincze, H.C. Lichtenegger, Photon energy becomes the third dimension in crystallographic texture analysis, Angewandte Chemie Int. Ed. 55 (40) (2016) 12190–12194.
[76] M. Liebi, M. Georgiadis, A. Menzel, P. Schneider, J. Kohlbrecher, O. Bunk, M. Guizar-Sicairos, Nanostructure surveys of macroscopic specimens by small-angle scattering tensor tomography, Nature 527 (7578) (2015) 349–352.

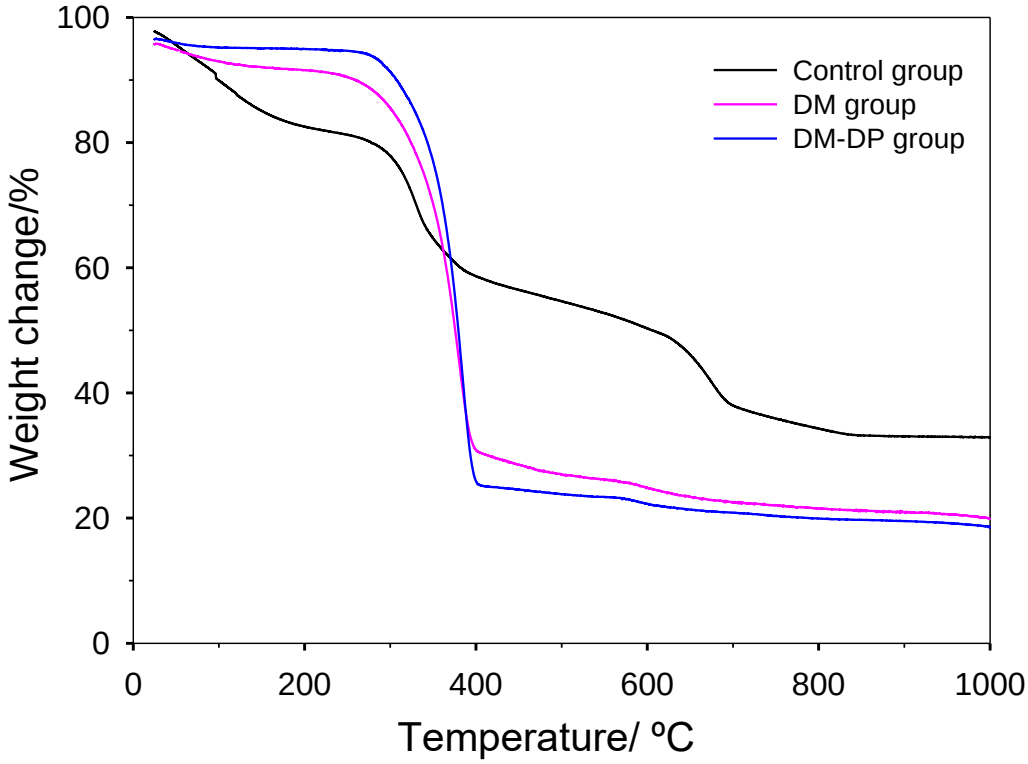

Figure S1. TGA curves of the cuticle samples from the three groups. Comparing control and DM groups shows that the mineral phase in the cuticle samples is removed (residual mineral phase at 1000 °C in control absent in DM and DM-DP), and slight differences between the DM and DM-DP groups.

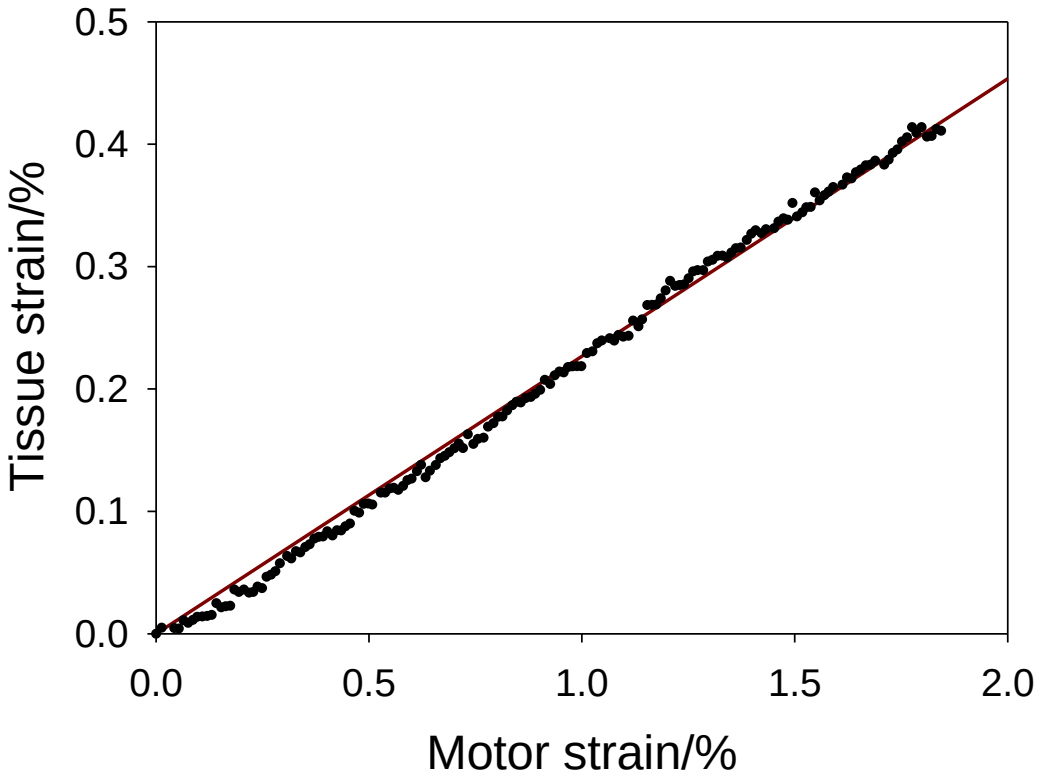

Figure S2. Representative plot of tissue strain as a function of motor strain, where the ratio of tissue strain to motor strain was obtained from the linear regression.

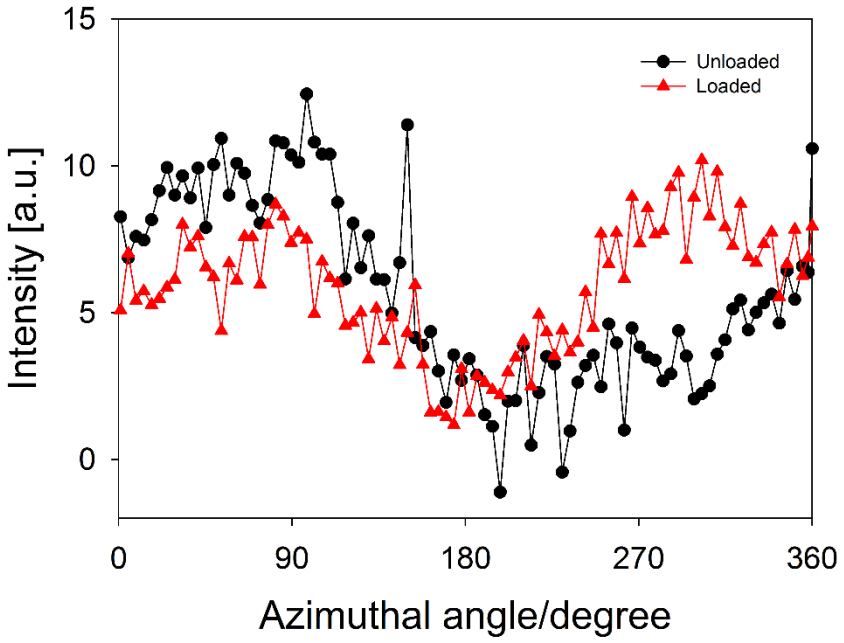

Figure S3. An example plot of (002) intensity as a function of the azimuthal degree (I(χ)) in unloaded (black circles) and loaded condition (red triangles) from control cuticle. Note that the unloaded profile too shows some degree of angular anisotropy, arising from the sample-tilt in 3 dimensions [1].

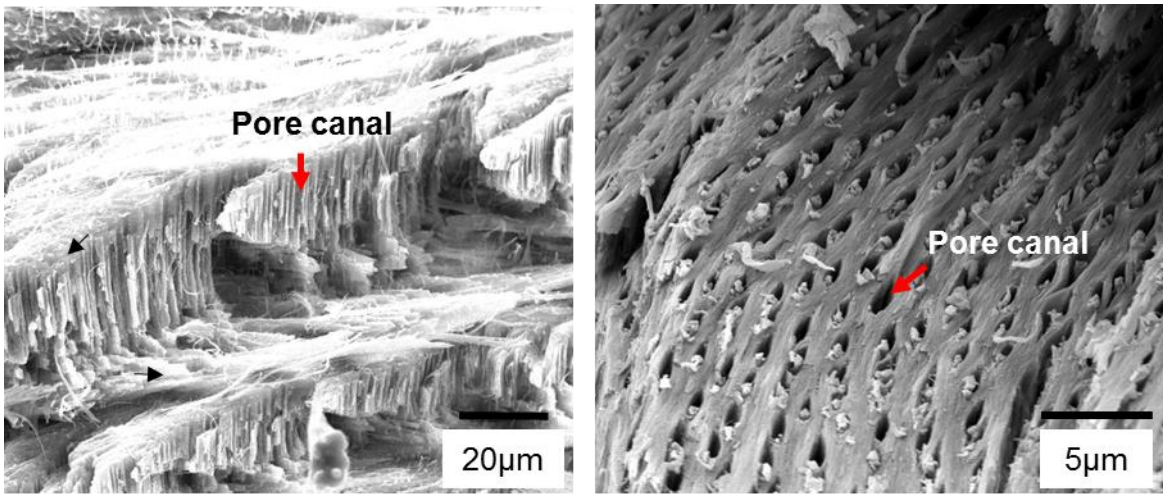

Figure S4. Scanning electron microscope images for fracture surfaces of tergite from stomatopod (mantis shrimp), showing (left) the stacked twisted plywood layers (indicated by black arrows) and (right) from a more vertical orientation, the pore canals (indicated by red arrows) and residual out-of-plane fibres in the pores, indicating a honeycomb structure [2] in the cuticle.

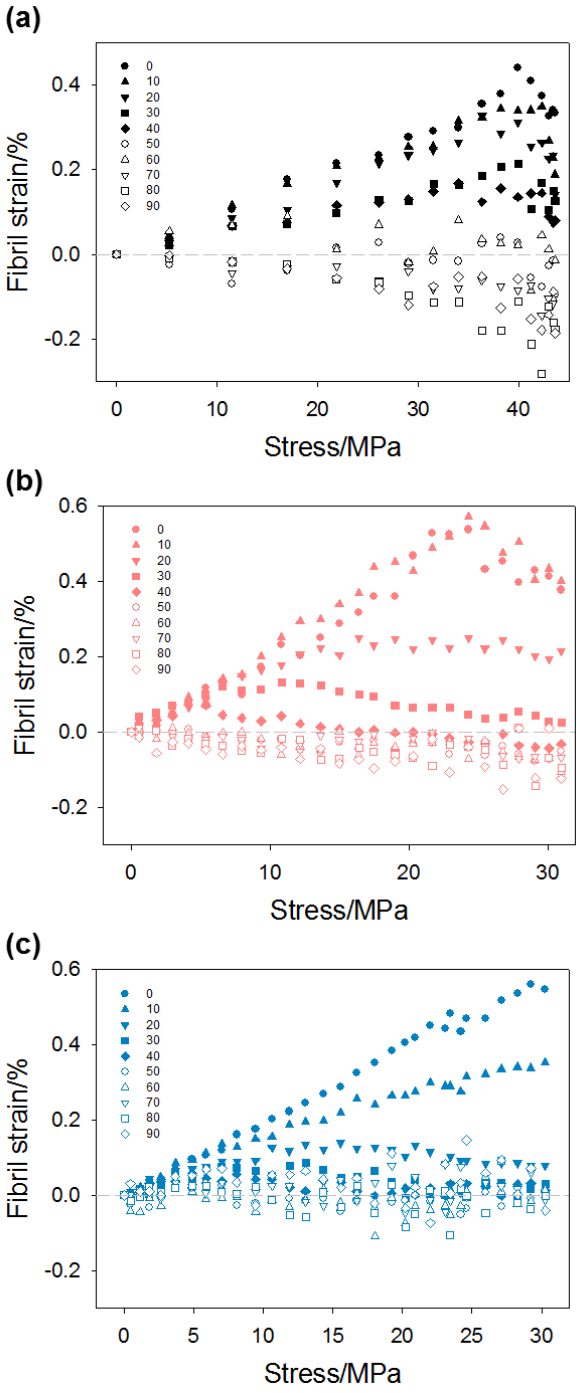

Figure S5. Representative angle-dependent variation in fibril strain changes of $D_{(002)}$, showing tensile (positive strain) for fibrils along the loading axis, changing to compressive (negative strain) fibrillar response for chitin fibrils away from the loading direction in the control group (a). It is observed that – relative to the control group – there is a higher positive strain, alongside a less negative strain (near non-deformation) in the DM (b) and DM-DP (c) groups.

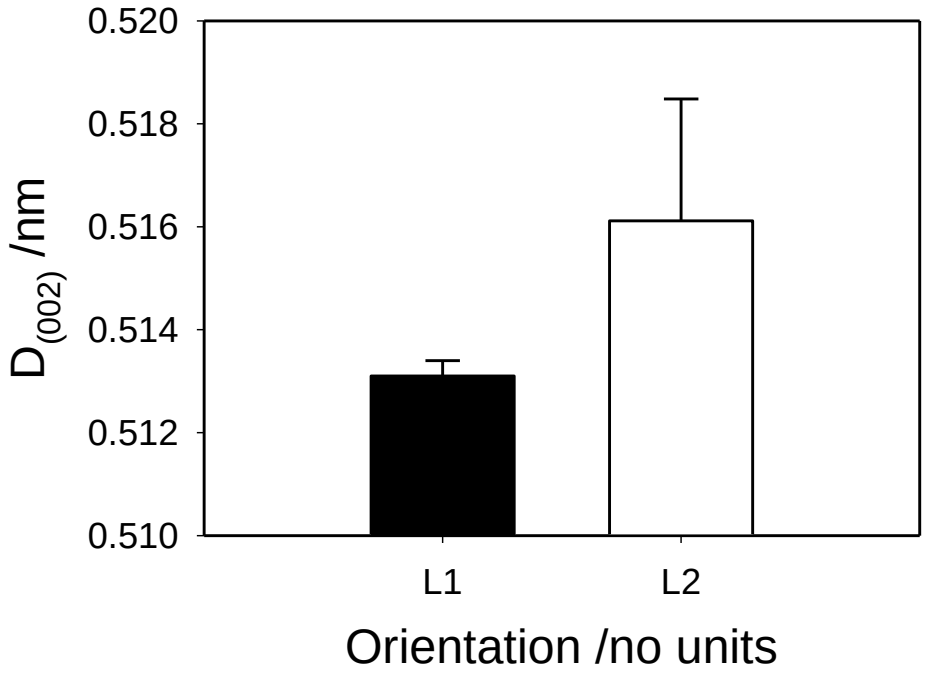

Figure S6. *Diffraction geometry effect*: Averaged $D_{(002)}$ in L2 configuration versus L1 configuration in tergite cuticle in control state. There is a spatial variation of $D_{(002)}$ across the exo- to endocuticle which accounts for the larger standard deviation in L2; L1 measurements are averaged across the thickness from the beginning so do not exhibit this feature.

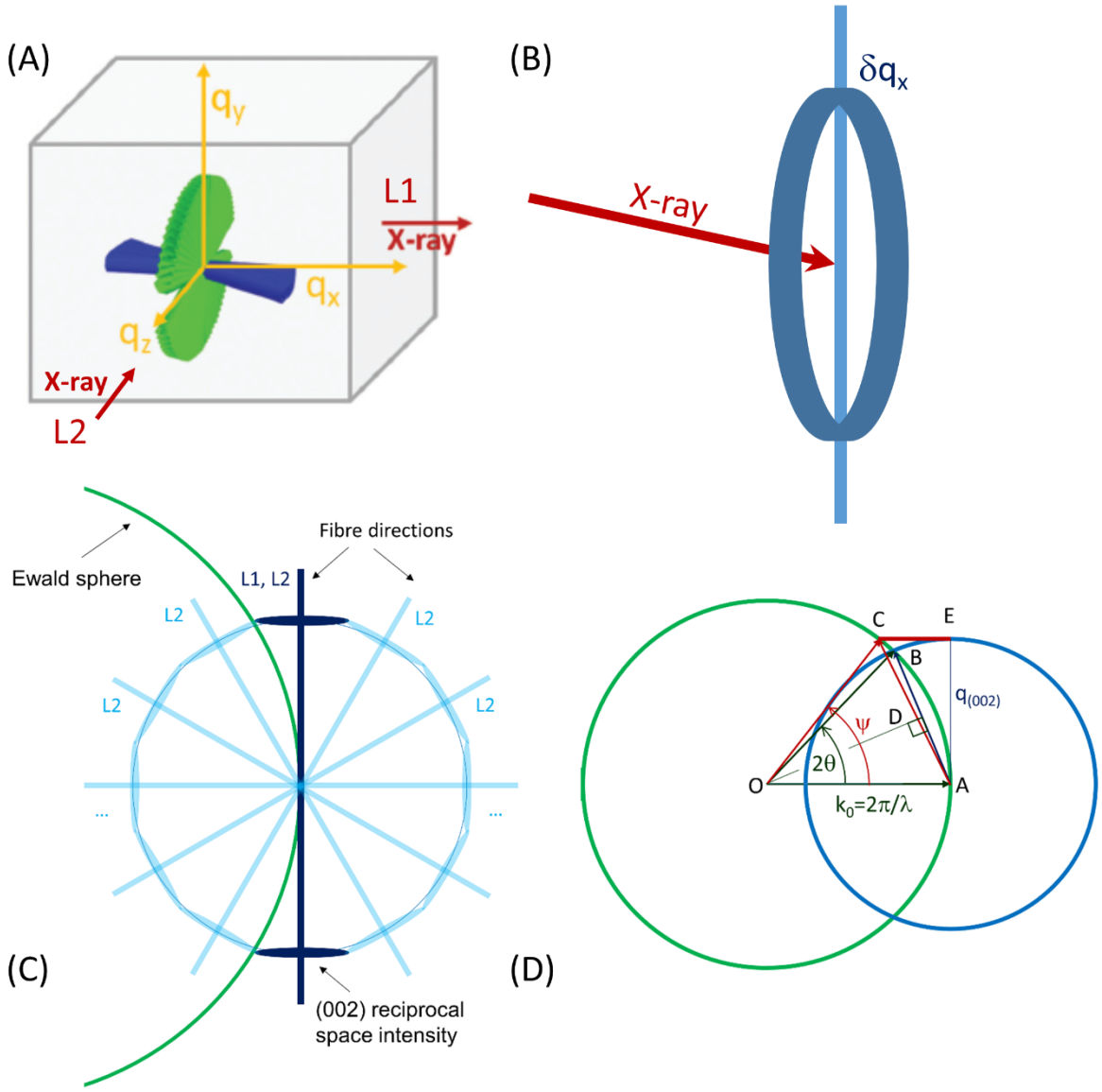

Figure S7: *Diffraction geometry schematic:* (A) Schematic representation of the in-plane Bouligand arrangement of fibres (green) and out-of-plane fibres (blue); image adapted from our prior work [1]. Two different diffraction geometries are shown: the beam normal to the Bouligand plane (L1; horizontal) and at 90° to the plane (L2: from lower left to upper right in perspective view) are shown. (B) Schematic representation of the band of intensity (dark blue) in reciprocal space, extended in q_x direction by δq_x, for a continuous Bouligand-type angular distribution of fibres. Beam direction is shown in L1-direction (red arrow). Vertical line indicates one fibre direction as example. (C) A 2D cutaway of the reciprocal space intensity distribution, showing Ewald sphere (green line) and two diffraction geometries – dark blue (L1) showing the intersection of the left tail of the reciprocal space band with the Ewald sphere and light blue (L2) showing multiple fibre orientations in this plane. (D) Idealised sketch of part of (C), showing dimensions of different lengths and calculation of the intersection in L1-geometry

(red arrow) and the equivalent scattering vector AC. The $q_{(002)}$ scattering vector is of length AB. Calculations are given below.

Diffraction geometry effect:

From the Ewald construction, it is seen that the lattice vector $d_{(002)} = 2\pi/q_{(002)}$, where $q_{(002)}$ = AB, as is well known. From the **Figure S7**, it can be seen that the intersection of the reciprocal space ellipsoid (for the vertically oriented fibril in L1-geometry) is at C, and that AC = 2 k_0 $\sin(\psi/2) = (4\pi/\lambda) \sin(\psi/2)$. Further, $\sin(\psi) = (q_{(002)}/(2\pi/\lambda))$. Writing AC in terms of an equivalent $d'_{(002)} = 2\pi/AC$, we have $d'_{(002)} = \lambda/(2 \sin(\arcsin(\lambda/d_{(002)}) /2))$. Note that as $\lambda \rightarrow 0$ or $k_0 \rightarrow \infty$, $d'_{(002)} = d_{(002)}$ in the small-angle limit. By using λ = 0.8856 Å and $d_{(002)}$ = 5.16 Å, we obtain $d'_{(002)}$ = 5.14 Å.

Figure S7 (C) compares L1 (dark blue) and L2 (light blue) fibre orientations: For the L2-geometry, fibres at all angles to the vertical with respect to the beam direction (due to the Bouligand fibre distribution), so for a fibre oriented at $2\theta/2$, the centre of the reciprocal space intensity ellipsoid will be at B, and the Bragg diffraction condition will be satisfied. For the L1-geometry, in contrast, all fibres are perpendicular to the beam; their angular distribution lies in the plane coming out perpendicular to the plane of the paper. Note also that the dark blue out-of-plane fibres in **Figure S7(A)** are too far away from the Ewald sphere intersection condition to contribute to the signal.

Supplementary Information – References:

[1] Y. Zhang, P. de Falco, Y. Wang, E. Barbieri, O. Paris, N.J. Terrill, G. Falkenberg, N. Pugno, H.S. Gupta, Towards in situ determination of 3D strain and reorientation in the interpenetrating nanofibre networks of cuticle, Nanoscale 9(31) (2017) 11249-11260.
[2] D. Raabe, P. Romano, C. Sachs, A. Al-Sawalmih, H.-G. Brokmeier, S.-B. Yi, G. Servos, H. Hartwig, Discovery of a honeycomb structure in the twisted plywood patterns of fibrous biological nanocomposite tissue, Journal of Crystal Growth 283(1) (2005) 1-7.

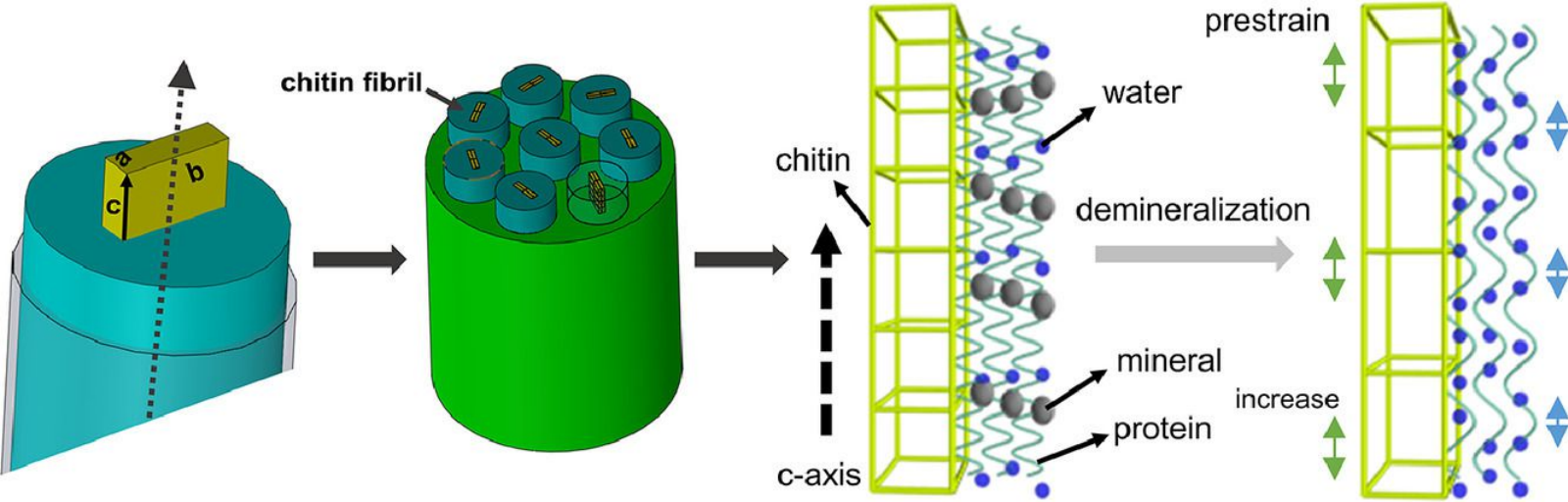
a
b
c
chitin fibril
chitin
water
demineralization
mineral
protein
c-axis
prestrain
increase